JOURNAL OF PROPULSION AND POWER
Vol. 25, No. 4, July–August 2009

Experimental Characterization of a Two-Phase Flowfield in a Solid Rocket Motor Model

B. Tóth* and J. Anthoine†
von Kármán Institute for Fluid Dynamics, 1640 Rhode-St-Genèse, Belgium
and
J. Steelant‡
ESA, 2200 AG Noordwijk, The Netherlands

DOI: 10.2514/1.40599

In solid propellant rocket motors incorporating a submerged nozzle, liquid alumina residues of the combustion can be entrapped in the cavity formed by the casing and the nozzle integration part. This continuous entrapment leads to an accumulation of slag, resulting in a considerable mass at the end of the booster operation. Various aspects of the slag accumulation are experimentally investigated using a simplified cold-gas model. The main focus is on the characterization of the internal flowfield by a new two-phase particle image velocimetry method in a representative cold-gas, two-phase flow configuration. The technique is based on a two-color YAG laser and phase separation methodology using fluorescent dyes. This approach permits the simultaneous separation of the images of the two phases by optical means. This new method opens a new dimension of experimental capabilities and two-phase numerical code validation. The investigation reveals two droplet-entrapment mechanisms for small and large droplets, respectively. Small droplets tend to follow approximately the gas flow and are therefore transported to the recirculation zone within the cavity and contribute to the accumulation. Large droplets follow a ballistic trajectory and can therefore be entrapped by the cavity due to their inertia. This also increases the amount of accumulated liquid in the slag pool.

Introduction

THE first stage of launch vehicles (e.g., Ariane 5, Vega, shuttle, H-II) generally consists of solid propellant rocket motors (SRMs). They operate during the first part of the liftoff, providing most of the thrust to accelerate the vehicle. To shorten the overall length, the nozzle is submerged into the last segment of solid propellant. This integration allows the vectoring of the nozzle throughout the launch trajectory. At the start, the convergent, the sonic throat, and a part of the nozzle divergent are surrounded by solid propellant. During combustion, the regression of the solid propellant surrounding the nozzle integration part leads to the formation of a cavity around the nozzle lip. The combustion process generates liquefied alumina droplets originating from the aluminum composing the propellant grain, which are carried by the hot combustion gases toward the nozzle. Meanwhile, the droplets interact with the vortices characterizing the internal flow; thus, they can modify their properties. As a consequence, some of the droplets are entrapped in the cavity instead of being exhausted through the throat. The amount of entrapped droplets in the cavity depends most probably on their interaction with the vortices. The accumulation of the droplets in the cavity generates an alumina puddle, also called slag. This slag reduces the performance of the solid propellant motor due to both its dead weight and its noncontribution to the impulse generation. In case of the solid propellant motors (moteurs à propergol solide, or MPS) of Ariane 5 (MPS P230), the total mass of the accumulated particles can reach up to 2 tons by the end of the launch [1].

Background

The slag accumulation in an aluminized SRM has already been studied in various projects. Many aspects of the driving mechanisms have already been pointed out, and each of these basic phenomena has been investigated.

First, the aluminum combustion and the alumina formation are described [2–5] and the generated alumina droplet size is predicted.

Once the droplets are in the flow, their transport is first investigated through quasi-steady numerical simulations [6–8]. However, as the unsteady nature of the internal flowfield is proven to be important [9,10]. Such investigations also highlighted that the slag accumulation and the pressure oscillation phenomena may be linked to each other [10,11]. To better understand the unsteady behavior, the different internal vortex generation phenomena are assessed [12–14].

As the droplets impact on any of the internal surfaces of the motor, the nature of the interaction and the behavior of the eventually forming liquid film (primarily on the nozzle lip) should be known [15,16], to see whether a droplet contributes to the slag or returns to the flow.

Finally, once the slag is deposited in the cavity, it may slosh inside its containment [17]. If the aerodynamic forces are strong enough (and/or combined with the sloshing), slag may be ejected through the nozzle. Though the onboard dead mass decreases in this case, the momentum impulse loss of the motor cannot be recovered. Furthermore, depending on the amount of ejected slag, thrust oscillations may occur, leading to control problems and possible vehicle instabilities [18]. Another consequence of the slag ejection is that the total amount of actually accumulated alumina might be higher than what is observed after a firing test or launch.

In spite of many predominantly numerical investigations of the slag accumulation and the internal flow in SRMs [19–22], the occurring processes are still not fully understood. There is no known model that can entirely describe the accumulation mechanism and

Presented as Paper 5050 at the 44th AIAA/ASME/SAE/ASEE Joint Propulsion Conference & Exhibit, Hartford, CT, 20–23 July 2008; received 27 August 2008; accepted for publication 5 April 2009.

*Postdoctoral Candidate, Environmental and Applied Fluid Dynamics Department, Chaussée de Waterloo 72; balazst@gmail.com. Student Member AIAA.

†Associate Professor, Environmental and Applied Fluid Dynamics Department, Chaussée de Waterloo 72. Member AIAA.

‡Senior Researcher, Technical and Quality Management Directorate, Aerothermodynamics and Propulsion Analysis Section, European Space Research and Technology Centre, Keplerlaan 1, P.O. Box 299; Johan.Steelant@esa.int. Member AIAA.

provide clear suggestions to designers to minimize the slag mass in future launchers. In addition, the available experimental observations are even more limited and, in the case of a real motor, they mostly provide slag [19] or internal pressure evolutions [23].

Objectives

The goal of the present study is to characterize experimentally the driving parameters of the slag accumulation in a nozzle cavity. The geometry of the MPS P230 of the Ariane 5 formed the basis for a scaled two-dimensional-like simplified cold-gas experimental model [24]. To achieve this objective, the interaction of the droplets (modelling the liquefied alumina droplets of the SRM) with the flow and the droplet entrapment process are investigated.

At first, the main parameters of the modeled accumulation process were investigated [25] experimentally. Further, the internal flowfield was characterized by performing single-phase particle image velocimetry (PIV) measurements [26]. These data were already used to validate three-dimensional large eddy simulations, and the numerical model was shown in two-phase flow configuration as well [27].

The current goal is to create a database by investigating experimentally the internal two-phase flowfield of the cold-gas model. On the one hand, the effect of droplets on the statistical flow properties is aimed for. On the other hand, some of the physical mechanisms acting during the interaction between the two phases are to be addressed. These objectives also involve the development of a two-phase PIV method allowing the experimental capture of the instantaneous velocity fields of the two phases separately.

Two-Phase Particle Image Velocimetry Approach

The optical whole-field PIV measurement technique determines the instantaneous velocity field in a plane.

In single-phase flow conditions, small (investigating air: $\sim$1-μm-diam oil) tracer particles are injected into the fluid. The tracers follow the motion of the fluid without disturbing it. The plane of interest is illuminated by a light sheet (in general, using a laser source). The tracers inside the sheet scatter light, from which two successive images with a known separation time (Δt) are recorded by a (generally, digital) camera. Therefore, by determining the local displacement of the tracer images ($\Delta \bar{s}$), the velocity of the flow can be easily obtained ($\bar{v} = \Delta \bar{s}/\Delta t$).

In practice, the image pairs are divided into smaller regions, called interrogation windows. In each window pair, the mean displacement of the tracer images is determined, basically by using the cross-correlation function. In the PIV algorithm of the von Kármán Institute, more elaborate methods (e.g., iterative window refinement, window overlapping, validation procedure, etc.) ensure a more precise displacement determination. More details about the conventional PIV technique [28] or about the algorithm [29] can be found in the literature.

During classical PIV application, generally the second harmonic of a YAG laser ($\lambda = 532$ nm) is used to generate the light sheet. However, when performing two-phase PIV experiments with air and liquid droplets, fluorescent material should be used. Kosiwczuk et al. [30] showed that a shorter illumination wavelength is needed and carried out experiments using the third harmonic of a YAG laser ($\lambda = 355$ nm). In this case, the illuminating wavelength is sufficiently short to use two different fluorescent dyes in the two phases. The dyes will emit light at two rather distinct bands of the visible spectrum above $\lambda = 355$ nm. Thus, using two cameras equipped with proper optical filters, the images of the two phases can be separated optically. Therefore, two images can be recorded simultaneously, which contain only one of the phases each. However, Kosiwczuk et al. [31] also showed that the optical separation might not be perfect, as some residual light might remain in one of the images originating from the other phase.

Currently, by keeping the idea of separating the two phases optically (see Fig. 1), the quality of the separation is improved. For this purpose, two different fluorescent dyes are dissolved in the

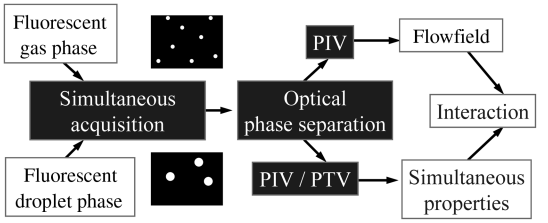

Fig. 1 Two-phase flow measurement principle.

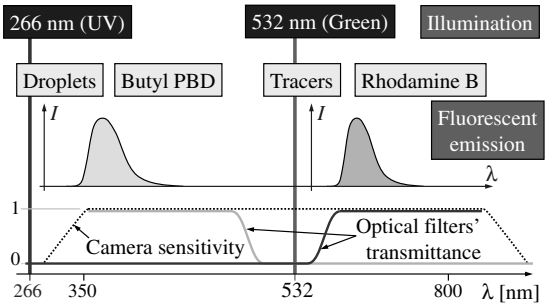

Fig. 2 Principle of the proposed measurement technique.

two phases (droplets and tracers). However, these dyes would be excited instantaneously by different wavelengths.

A schematic of the principle of the proposed technique can be seen in Fig. 2. As an illumination source, a YAG laser is applied, which is capable of producing pulses at the second ($\lambda = 532$ nm) and fourth ($\lambda = 266$ nm) harmonic simultaneously. The idea is that the two pulses are exciting fluorescent dyes, which have high absorbance at only one of the wavelengths (rhodamine b at $\lambda = 532$ nm and butyl pbd at $\lambda = 266$ nm). Therefore, the two phases would emit light at very distinct bands of the spectrum. Finally, by using two cameras equipped with proper optical filters, only the light of the fluorescent emissions is recorded.

As Kosiwczuk et al. [30] showed, the use of fluorescent droplets does not affect the image formation. As long as the image pairs of the tracers and the droplets are separated and processed with a classical PIV algorithm, the measurement uncertainty is not affected either.

More details about the technique are given by Tóth and Anthoine [32].

Experimental Conditions

The geometry of the cold-gas experimental model simulates the main characteristic features of the SRM of the Ariane 5. It was introduced and explained by Tóth et al. [25,26]. In Fig. 3, the test section is shown, which is attached to a vertical wind tunnel. Therefore, gravity is aligned with the longitudinal (x) axis.

The model is designed in a way that allows the use of optical measurement techniques (such as PIV) to characterize the internal flowfield. Therefore, most of the walls are made of planar transparent material. Furthermore, different geometrical parameters (inhibitor height and position, nozzle throat opening, cavity width) can be

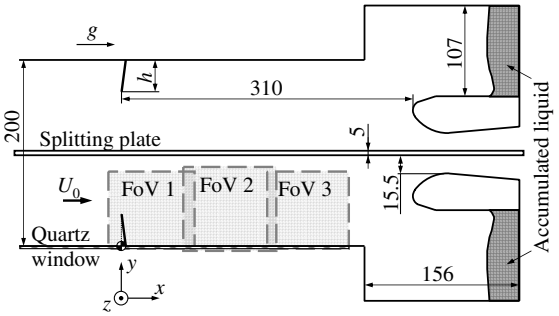

Fig. 3 Geometry of the test section and the FoVs during the two-phase PIV experiments.

varied. However, currently only the nominal configuration (see Fig. 3, where $h = 33.5$ mm) is investigated, which represents the best the geometry of the P230 motor [26].

The square (200×200 mm^2) test section has a symmetric arrangement. The inhibitor between the second and the third segments of the MPS P230 is modeled by a pair of inclined obstacles. The presence of this inhibitor induces vortex generation, called obstacle vortex shedding (OVS). To prevent any interaction between the two OVS created downstream of both inhibitors, the test section is separated by a splitting plate. Furthermore, to allow vortices to reach the nozzle head as in the real configuration, the inhibitor is placed $9h$ from the nozzle tip in the present configuration. Because the model has a symmetric arrangement and, therefore, a symmetric flow condition (which has been verified), the measurements are carried out using only one side of the test section.

The model of the submerged nozzle, including the model of the appearing cavity, is installed at the outlet of the test section. The setup is designed for subsonic operation. Therefore, the sonic condition at the nozzle of the real case is not respected. Moreover, it is not the goal of the present study to perfectly model the real conditions, but rather to focus on basic phenomena, such as a vortex shedding, the two-phase flow aspect, and the fundamental mechanisms leading to liquid accumulation in stagnant areas.

The experiments are carried out at room temperature using air to model the gas phase of the internal fluid of the SRM and using droplets of mainly water to model the alumina droplets. For security (toxic materials) and optical (droplet deposition on the lateral walls) reasons, the liquid flow rate has to be kept low. Therefore, a bulk air velocity of $U_0 = 2$ m/s was chosen, corresponding to a $Re_h = 5025$. This Reynolds number is substantially lower than in the case of the real motor. Nevertheless, by respecting the turbulent flow regime, the viscous effects remain similarly negligible. Evaluating the effect of these conditions on the vortical structures in the real motor and the cold-flow test setup is difficult. Without side injection in a two-dimensional-like geometry, the authors do not believe that a full flow similarity could be achieved, even at higher reference velocities.

The droplet phase is generated by a spray device (based on a Lechler 156.000.17.13 model), which is mounted in the middle of the stagnation chamber of the wind tunnel. The atomizer is supplied by $p_{\text{liq.}} = 0.8$ bar liquid and $p_{\text{air}} = 1.25$ bar air pressures. These conditions provide a flow rate of about $\dot{Q}_{Vd} = 0.133$ l/min. The generated droplet-size distribution is characterized by phase Doppler anemometry measurements using water. A mean Sauter droplet diameter of $d_{32} = 106.2$ μm is obtained, with a distribution ranging from about 30 to 245 μm. These parameters provide a Stokes number of about $St = 2.33$ and a volume fraction of $\alpha_p = 0.4 \times 10^{-4}$. The nondimensional parameters in the case of the P230 motor are about $St = 6$ and $\alpha_p = 2.2 \times 10^{-4}$. By recalculating the equivalent droplet diameter in the motor, the models represent a distribution of about $d = 14.3$–116.6 μm with a mean diameter of about $d_{32} = 50.5$ μm. This corresponds roughly to the second peak of the bimodal lognormal droplet-size distribution of the P230 motor. The first lobe represents the majority of the droplet mass in the submicron range. These submicron droplets are assumed to follow the flow perfectly, and their contribution to the agglomeration process is neglected due to the short overall length of the current cold-gas model. Therefore, they are neglected in the present experiment.

The illuminating YAG laser operates at 9.22 Hz. To ensure a simultaneous image recording, the two cameras acquire an image pair only at every third laser double pulse. This results in an acquisition rate of about 3.07 Hz. Among the settings of the cameras, 2×2 pixels^2 binning is selected to gain sensitivity and to respect the desired acquisition rate. Therefore, both of the image pairs have a 640×432 pixels^2 resolution.

As Fig. 3 indicates, altogether three fields of view (FoVs) are defined to cover the area of the test section, which is accessible with the UV laser beam through a quartz window. In each FoV, 1200–1700 two-phase image pairs are recorded with both cameras in series of 100 samples. Between the series, the test section is cleaned to reduce the effect of the deposited droplets. After the two-phase acquisitions, a series of 1200–1700 image pairs are recorded in single-phase flow configuration as a reference, to see the effect of droplets on the flowfield.

Experimental Results

Once the image pairs are processed with the PIV algorithm, the instantaneous velocity fields are averaged to obtain the mean flow properties and turbulence quantities.

Resulting Statistical Flowfields

The distribution of the measurement quality is shown in Fig. 4 together with the streamlines of the flow. During the evaluation of the results, the regions where $SN_{\text{mean}} < 2$ should be handled with great care, as the observed information might have no physical content due to the low measurement quality.

Focusing on the air-phase flowfields represented by the streamlines, a similar recirculation region is revealed downstream of the inhibitor for the single- and two-phase flow conditions, as previously observed by Tóth et al. [26] and Lema et al. [27] at higher Reynolds numbers. A main circulating structure is created by the separating flow, which extends from the inhibitor tip. Unfortunately, its downstream end falls outside the investigable area. Therefore, it is not known whether the flow reattaches before the cavity entrance. By analyzing the captured part of the recirculation region, the main bubble appears to be flatter in the two-phase flow case (see Fig. 4b) than in the single-phase flow case (see Fig. 4a). As already seen during a previous computational fluid dynamics study [27], the primary effect of the droplets on the mean flowfield is the flatter main recirculation bubble.

Furthermore, the center of the main recirculation bubble shifts about $0.3h$ upstream in the two-phase flow condition (Fig. 4b) with respect to the single-phase flow case (Fig. 4a). As the main bubble is compressed, the secondary counter-rotating mean structure at the downstream corner of the inhibitor becomes smaller as well.

The mean droplet-phase flowfield analyzed by the PIV algorithm is shown in Fig. 4c. The field can be divided into two regions. On the one hand, a mean pattern similar to the air phase can be observed at about $Y/h \leq 1$, drawn by small droplets, which are able to follow better the airflow. On the other hand, at $Y/h > 1$, the whole range of the injected droplet sizes are present, including the large droplets. Their displacement governs the cross-correlation results. Therefore,

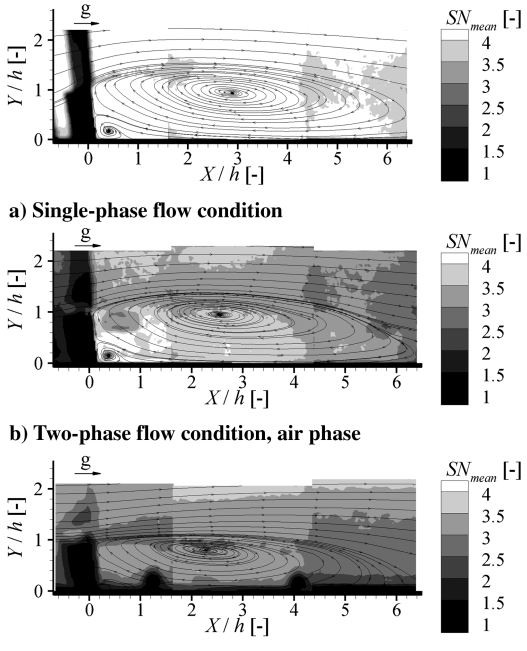

a) Single-phase flow condition

b) Two-phase flow condition, air phase

c) Two-phase flow condition, droplet phase

Fig. 4 Measurement quality and mean flowfield.

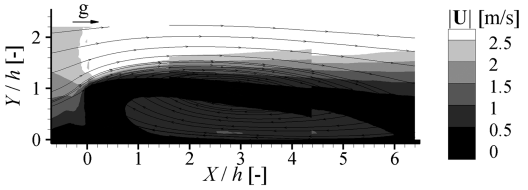

a) Single-phase flow condition

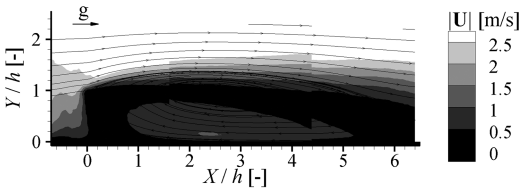

b) Two-phase flow condition, air phase

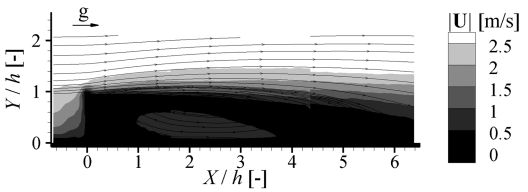

c) Two-phase flow condition, droplet phase

Fig. 5 Velocity magnitude distribution.

in this region, the measured velocity primarily represents the motion of the large droplets. Because they are weakly affected by the airflow, the velocity field at $Y/h > 1$ is considerably different from the one observed in the air phase.

The contour plots of the velocity magnitudes are shown in Fig. 5. In the regions where the measurements are reliable, only slight differences can be observed between the single- and the two-phase configurations.

In the figures, the edges of the FoVs are visualized by the discontinuity of the contour plot. It is the most pronounced between FoVs 2 and 3. In FoV 3, the air velocity appears to be substantially higher than in FoV 2. The differences originate from the fact that the nominal flow velocity is rather low ($U_0 = 2$ m/s), which is difficult to measure accurately in the wind tunnel. To quantify the velocity mismatch, a $|\mathbf{U}|$ profile is extracted along $Y/h = 2$ (in the freestream). The profile is shown in Fig. 6, in which a difference of about 17% is measured at the discontinuity between FoVs 2 and 3 and of 2% between FoVs 1 and 2. Therefore, the reference velocity could be considered to be affected roughly by the same amount.

In the following paragraphs, the turbulence intensity (TI) of the in-plane velocity components is determined. TI_U and TI_V are obtained by normalizing the standard deviation of the corresponding velocity component by the actual freestream velocity, U_0.

Concerning the transversal fluctuations of the continuous phase, a slight turbulence decay (around 20% lower) can be observed in the two-phase flow configuration with respect to the single-phase flow results (see Figs. 7b and 7a).

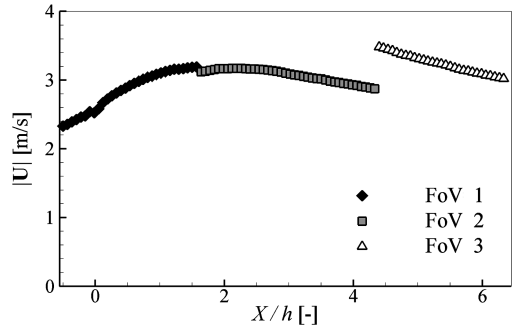

Fig. 6 Velocity magnitude profile ($|\mathbf{U}|$) at $Y/h = 2$.

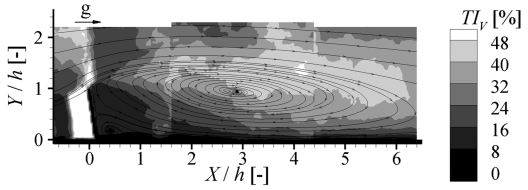

a) Single-phase flow condition

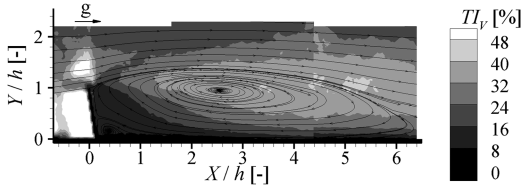

b) Two-phase flow condition, air phase

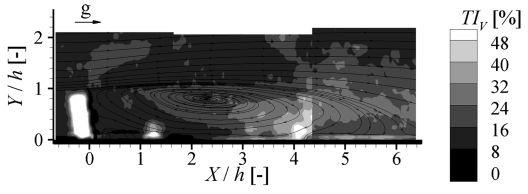

c) Two-phase flow condition, droplet phase

Fig. 7 Transversal velocity component fluctuation.

However, looking at Fig. 7c, in the droplet-phase motion, a considerably lower fluctuation can be seen compared with the TI_V levels of the corresponding air motion (around 50% lower). These observations again seem to be in good agreement with the longer characteristic time of the droplets, which are not able to follow the high-frequency changes of the air phase; therefore, they might also damp the fluctuations of the air.

Furthermore, one should note that the meaning of the droplet-phase fluctuation is not entirely analogous to the carrier-phase fluctuations. Especially below the inhibitor shear layer, where the freestream flow separates and creates a low-velocity recirculation, the larger droplets travel at a considerably higher velocity, as they are unable to adapt rapidly to the low-velocity fluctuations. On the other hand, the smaller droplets may adapt more quickly to the local

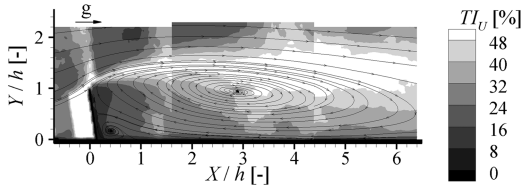

a) Single-phase flow condition

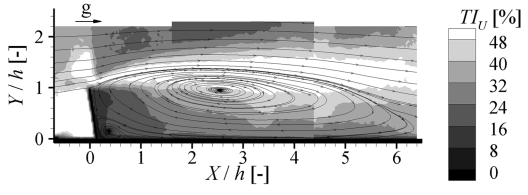

b) Two-phase flow condition, air phase

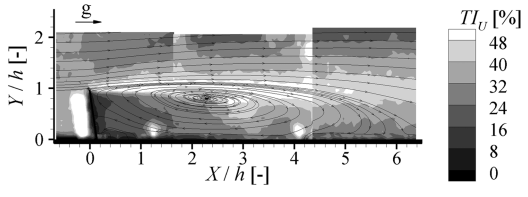

c) Two-phase flow condition, droplet phase

Fig. 8 Longitudinal velocity component fluctuation.

low-speed conditions and to the continuous phase fluctuations as well. Therefore, in the droplet-phase samples, different velocity information may be present at the same location depending on the actual droplet diameter, which may also influence the local velocity fluctuation during the statistical analysis.

The patterns of the fluctuations of the longitudinal velocity component (TI_U) seem to be even more similar in general between Figs. 8a and 8b. However, in the shear layer region ($0 < X/h < 2.5$), the turbulence peak values appear to be slightly higher and more spread out in two-phase flow condition. This might be explained by the fact that, although the air phase accelerates in the vena contracta, the droplets are not able to adapt to the flow change. Because the droplets are randomly distributed in the domain, when the local droplet concentration is higher, they may limit the acceleration of the air; when the local droplet concentration is lower, the air might be able to accelerate freely. As a consequence, at any points around and in the shear layer, due to the temporal variation of the droplet concentration, lower and higher air velocities are expected instantaneously, which obviously increases the longitudinal TI component.

Unlike the transversal turbulence intensity, the longitudinal velocity fluctuation of the droplets shows similar levels (see Fig. 8c) to those of the continuous phase. However, the pattern is still different from the air phase. Here, the high-fluctuation area is approximately following $Y/h = 1$, instead of the curvature of the vena contracta. This pattern could show the mixing region, where the smaller droplets could start to enter the recirculation region.

Mean Relative Motion Between the Two Phases

The previous section showed that the differences between the mean air-phase motion and the mean droplet-phase motion are not always obvious. To be able to highlight them better, the two-phase flow plots described earlier are interpolated to a common rectangular grid (containing 150×50 cells) and all the droplet-phase quantities are subtracted from the air-phase quantities. These new variables are indicated by an "a–d" (air–droplets) index of Figs. 9 and 10.

Concerning the mean velocity differences between the continuous phase and the droplets, on the one hand, the transversal component (see Fig. 9b) shows a low-amplitude deviation, which is caused mainly by the lack of a vena contracta in the droplet-phase mean flowfield. On the other hand, the pattern of the longitudinal velocity component difference (see Fig. 9a) clearly shows that, in the region where the mixing of the droplets should take place, the air phase has a substantially lower velocity, especially close to the tip of the inhibitor (in the top part of the main recirculation bubble). Because the large droplets require a longer time to respond to the air-phase fluctuations, they are not able to follow the streamlines of the vena contracta. Instead, they cross the curved shear layer and enter with a high velocity into the low-speed recirculation area.

Because the mean longitudinal velocity component difference is more important than the transversal velocity component difference, by subtracting the mean velocity magnitude of the droplet phase from the air-phase data, the resulting contour plot (see Fig. 9c) resembles Fig. 9a.

The turbulence intensity differences are shown in Fig. 10. Because the transversal velocity component fluctuation of the droplet phase is uniformly low (see Fig. 7c), the pattern of the fluctuation difference (shown in Fig. 10b) is similar to the pattern of the air-phase transversal fluctuation (see Fig. 7b).

However, the difference of the mean longitudinal velocity component fluctuations (indicated in Fig. 10a) shows, downstream of the inhibitor tip, both the slightly curved shear layer of the airflow and the high-fluctuation region of the droplet phase at $Y/h = 1$ (seen in Fig. 8c). The latter is visible roughly up to $X/h = 4$. It can be observed that these two areas are rather distinct spatially. Further downstream, in the wake of the inhibitor, the longitudinal turbulence intensity component, similar to the transversal component, shows a superior air-phase turbulence content.

By subtracting the magnitudes of the velocity fluctuation of the droplet phase from the air phase (indicated in Fig. 10c), all the structures described earlier appear: the mixing layer of the droplet phase is visible together with the one of the air-phase shear layer, which is followed by the wake of the inhibitor.

Discussions

The experimental results clearly highlight the importance of the droplet size on the behavior of the discrete phase.

The motion of the largest droplet classes should be studied carefully upstream of the inhibitor. Their trajectory may not be influenced significantly by the turbulent flow between the inhibitor and the nozzle cavity. Additionally, through agglomeration, their inertia may further increase. For similar reasons, one should investigate the potential of liquid accumulation on the upstream face

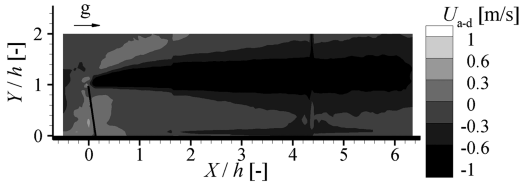

a) Longitudinal velocity component

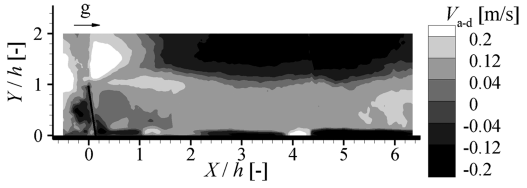

b) Transversal velocity component

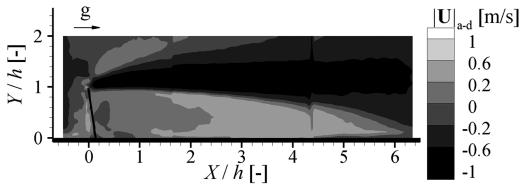

c) Velocity magnitude

Fig. 9 Velocity component differences (air droplets).

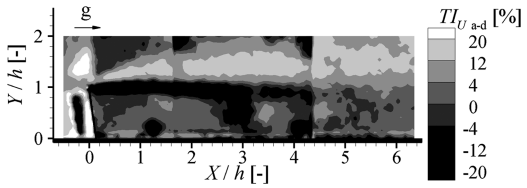

a) TI of the longitudinal velocity component

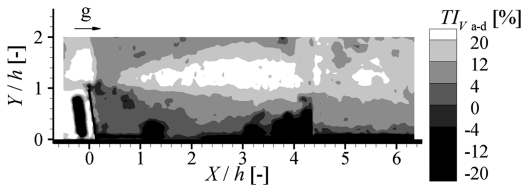

b) TI of the transversal velocity component

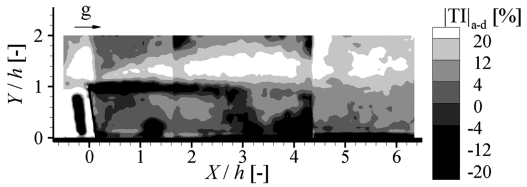

c) Absolute TI

Fig. 10 Turbulence intensity differences (air droplets).

of the inhibitor. This place may be the source of very large drops, which may gather momentum during launch, experiencing a larger gravity environment and falling directly into the nozzle cavity. As they represent a large volume, their contribution to the accumulation can be nonnegligible, despite their relatively low number count. Hence, they are not expected to globally modify the flow properties, and vice versa.

The smallest droplet classes (micron and submicron size) follow the flow, similar to the tracers employed in the PIV technique. Therefore, they are expected to be distributed quasi homogeneously in the combustion chamber. As all the streamlines of the gas phase have to leave through the nozzle, their direct contribution to the accumulation process is not deemed to be significant. Similar to the large droplets, in their presence no interaction is expected between the two phases.

The behavior of the intermediate droplet classes proved to be more complex. They have a limited ability to be influenced by the continuous phase. Furthermore, as their quantity may be sufficiently high, they may also modify the streamlines of the gas, leading to a two-way coupling situation. Although they may modify the energy and the properties of the vortical structures, a substantial change in the flowfield, such as the destruction of vortices, is not expected, as these flow structures are known to be present at the nozzle head from pressure oscillation studies (both in the real motor and representative scaled cold-gas tests). Therefore, the behavior of liquid phase in the vicinity of the vortices should be analyzed first.

Because of the centrifugal forces, the intermediate-size droplets are transferred away from the core of the vortices. However, as they respond to the local perturbations, the droplets may encircle the vortical flow structures. A mixing downstream of the inhibitor was shown in the cold-gas experiments, which is similar to the dispersion of the droplets originating from the segment(s) upstream of the inhibitor. If these droplets reside in the vicinity of the vortices, they may be deviated toward either the nozzle throat or the cavity once the flow structures interact with the nozzle head. This latter situation is meant to be the entrapment process. In the real motor, a two-phase flow is injected radially up- and downstream of the inhibitor. As a consequence, no mean recirculation bubble exists. However, this Taylor flow promotes the creation of vortices, prolongs their lifetime, and, therefore, potentially increases the residence time of the droplets in their vicinity. At the level of the nozzle, the total amount of liquid droplets is about double that at the inhibitor. As a consequence, a quasi-uniform droplet distribution is expected around the vortical structures, with the spatial distribution with respect to the vortex core strongly determined by the droplet diameter.

During the entrapment process, the largest classes are expected to impact on the nozzle head. The final fate of this liquid depends on the liquid film behavior on the nozzle lip. The relatively smaller classes may enter the cavity with the gas phase. However, as they are not able to perfectly follow the streamlines of the flow, a large number of them may hit one of the cavity walls. As a consequence, they form a liquid film and, eventually, a liquid pool. This entrapment mechanism is deemed to be the most important contributor to the slag accumulation in the P230 motor, due to the generation of large amounts of intermediate-size droplets.

Conclusions

The flow behavior within a scaled SRM combustor model has been statistically analyzed based upon a new two-phase PIV method. It consists of a laser producing pulses simultaneously at two different wavelengths. The excitation of two different fluorescent dyes by each of the laser wavelengths allows the simultaneously recording of the gas and droplet velocity fields.

Because of the measurement conditions, the reference velocity had to be decreased (from 10 to 2 m/s) with respect to the previous research [24]. Furthermore, the optical access currently allows only the investigation of the region of the main recirculation bubble downstream of the inhibitor. Nevertheless, the droplet-phase interaction results in similar modifications on the mean flowfield as predicted by the numerical simulations [27]. However, experimentally, the differences between the single- and two-phase cases are more pronounced (e.g., the main recirculation bubble is more affected in the presence of droplets).

Using the two-phase flow experimental database, smaller droplets are found in the recirculation zone downstream of the inhibitor. They appear to closely follow the air phase, demonstrating the mixing capability of the smaller droplet classes. However, near the inhibitor shear layer where large number of big droplets are located, a large velocity difference (above 1 m/s) is found, which decays slowly. This shows the importance of the inertia of the large droplets during the entrapment process.

Overall, the experiments revealed two mechanisms leading to slag accumulation. On the one hand, the smaller droplets (representing a short characteristic time) are able to respond to the fluctuations of the continuous phase. They are able to mix in the recirculation zone, to be carried by the vortical structures of the flow, and, finally, to be entrapped in the cavity. On the other hand, the large droplets (representing a long characteristic time) are not significantly affected by the airflow. Therefore, due to their inertia, they may fall into the cavity pool. The contribution of these large droplets to the liquid accumulation depends on the direction of their velocity vector when they pass in front of the inhibitor tip.

Future work should focus on the details of the instantaneous flow behavior and the evolution of the slag accumulation due to fuel regression throughout the SRM operation. Also, the effects of inhibitor deflection, grain size, finocyl configuration, etc., have a distinct impact on the droplet-gas interaction and deserve further attention.

Acknowledgment

This study has been supported by the European Space Agency through the General Support Technology Programme, activity number C51.MPA-818.

References

[1] "Internal Aerodynamics in Solid Rocket Propulsion," *RTO AVT/VKI Special Course*, edited by J. Anthoine, and P. Kuentzmann, von Kármán Institute, Rhode-Saint-Genèse, Belgium, May 2002.

[2] Beckstead, M. W., "A Model for Solid Propellant Combustion," *Proceedings of the 14th JANNAF Combustion Meeting*, John Hopkins Univ., Baltimore, MD, 1977.

[3] Cohen, N. S., "A Pocket Model for Aluminum Agglomeration in Composite Propellants," *AIAA Journal*, Vol. 21, No. 5, 1983, pp. 720–725.
doi:10.2514/3.8139

[4] Duterque, J., and Lambert, D., "Synthèse des Travaux sur l'Agglomération de l'Aluminium dans le Propergol du MPS P230," 3*ème* *Colloque R&T CNES/ONERA "Ecoulements Internes en Propulsion Solide"*, Vol. 2, ONERA, Châtillon, France, March 1998, pp. 109–118.

[5] Jackson, T. L., Najjar, F., and Buckmaster, J., "New Aluminum Agglomeration Models and Their Use in Solid-Propellant-Rocket Simulations," *Journal of Propulsion and Power*, Vol. 21, No. 5, 2005, pp. 925–936.
doi:10.2514/1.11888

[6] Pevergne, T., and Le Helley, P., "Simulation Numérique des Impacts de Particules et Dudépôt dans le MPS P230," 3*ème* *Colloque R&T CNES/ONERA "Ecoulements Internes en Propulsion Solide,"* Vol. 2, ONERA, Châtillon, France, March 1998, pp. 201–210.

[7] Cesco, N., Dumas, L., Hulin, A., Pevergne, T., and Fabignon, Y., "Stochastic Models to the Investigation of Slag Accumulation in a Large Solid Rocket Motor," AIAA Paper 1997-3118, July 1997.

[8] Wirzberger, H., Macales, Y., and Yaniv, S., "Prediction of Slag Formation in a Solid Rocket Motor," AIAA Paper 2005-4488, July 2005.

[9] Godfroy, F., and Guéry, J.-F., "Unsteady Eulerian Flow Analysis of Solid Rocket Motor Slag," AIAA Paper 1997-2859, July 1997.

[10] Le Helley, P., Coste, S., and Pevergne, T., "Influence of the Unsteady Flow on the Alumina Flux Impinging the Nozzle and the Aft Dome of the Ariane 5 Booster," *2nd European Conference on Launcher Technology*, ESA, Noordwijk, The Netherlands, Nov. 2000.

[11] Dupays, J., "Two-Phase Unsteady Flow in Solid Rocket Motors," *Aerospace Science and Technology*, Vol. 6, No. 6, 2002, pp. 413–422.
doi:10.1016/S1270-9638(02)01182-3

[12] Vuillot, F., "Vortex-Shedding Phenomena in Solid Rocket Motors," *Journal of Propulsion and Power*, Vol. 11, No. 4, 1995, pp. 626–639. doi:10.2514/3.23888

[13] Traineau, J. C., Prévost, M., Vuillot, F., Le Breton, P., Cuny, J., Preioni, N., and Bec, R., "A Subscale Test Program to Assess the Vortex Shedding Driven Instabilities in Segmented Solid Motors," AIAA Paper 1997-3247, July 1997.

[14] Lupoglazoff, N., and Vuillot, F., "Parietal Vortex Shedding as a Cause of Instability for Long Solid Propellant Motors. Numerical Simulations and Comparisons with Firing Tests," AIAA Paper 1996-0761, Jan. 1996.

[15] Vardelle, M., Escure, C., Fauchais, P., Platet, B., and Lavergne, G., "Impact of Alumina Droplets on Cold and Hot Surfaces," *2nd European Conference on Launcher Technology*, ESA, Noordwijk, The Netherlands, Nov. 2000.

[16] Zaleski, S., and Gueyffier, D., "Simulation de l'Impact de Gouttes sur des Films Liquides," $3^{ème}$ *Colloque R&T CNES/ONERA "Ecoulements Internes en Propulsion Solide,"* Vol. 2, ONERA, Châtillon, France, March 1998, pp. 221–230.

[17] Meyer, R. X., "Coning Instability of Spacecraft During Periods of Thrust," *Journal of Spacecraft and Rockets*, Vol. 33, No. 6, 1996, pp. 781–788. doi:10.2514/3.26838

[18] Dotson, K. W., Murdock, J. W., and Kamimoto, D. K., "Launch Vehicle Dynamic and Control Effects from Solid Rocket Motor Slag Ejection," *Journal of Propulsion and Power*, Vol. 15, No. 3, 1999, pp. 468–475. doi:10.2514/2.5450

[19] Salita, M., "Deficiencies and Requirements in Modeling of Slag Generation in Solid Rocket Motors," *Journal of Propulsion and Power*, Vol. 11, No. 1, 1995, pp. 10–23. doi:10.2514/3.23835

[20] Fabignon, Y., Guéry, J.-F., Godfroy, F., Le Helley, P., Hylkema, J., Jacques, L., Lavergne, G., and Villedieu, P., "Slag Accumulation in Large Segmented Solid Motors with a Submerged Nozzle," *2nd European Conference on Launcher Technology*, ESA, Noordwijk, The Netherlands, Nov. 2000.

[21] Telara, M., Paglia, F., Stella, F., and Giangi, M., "Ariane 5 P230 SRM Frontal Thermal Protection Evolution: Numerical Simulation," AIAA Paper 2006-5242, July 2006.

[22] Najjar, F. M., Haselbacher, A., Balachandar, S., and Moser, R. D., "Simulations of Droplet Nozzle Impact and Slag Accumulation in the RSRM," AIAA Paper 2006-4588, July 2006.

[23] Fabignon, Y., Dupays, J., Avalon, G., Vuillot, F., Lupoglazoff, N., Casalis, G., and Prévost, M., "Instabilities and Pressure Oscillations in Solid Rocket Motors," *Aerospace Science and Technology*, Vol. 7, No. 3, 2003, pp. 191–200. doi:10.1016/S1270-9638(02)01194-X

[24] Tóth, B., Lema, M. R., Anthoine, J., and Steelant, J., "Assessment of Slag Accumulation in Solid Rocket Boosters: Summary of the VKI Research," AIAA Paper 2007-5760, July 2007.

[25] Tóth, B., Lema, M. R., Anthoine, J., and Steelant, J., "Assessment of Slag Accumulation in Solid Rocket Boosters: Part II, Two-Phase Flow Experiments," AIAA Paper 2006-4430, July 2006.

[26] Tóth, B., Lema, M. R., Steelant, J., Anthoine, J., and Rambaud, P., "Assessment of Slag Accumulation in Solid Rocket Boosters: Part I, Single-Phase," AIAA Paper 2005-4489, July 2005.

[27] Lema, M. R., Rambaud, P., Anthoine, J., and Steelant, J., "Assessment of Slag Accumulation in Solid Rocket Boosters: Part III, Two-Phase Flow CFD," AIAA Paper 2006-4431, July 2006.

[28] Adrian, R. J., "Particle-Imaging Techniques for Experimental Fluid Mechanics," *Annual Review of Fluid Mechanics*, Vol. 23, 1991, pp. 261–304.doi:10.1146/annurev.fl.23.010191.001401

[29] Scarano, F., "Particle Image Velocimetry Development and Application; Investigation of Coherent Structures in Turbulent Flows," Ph.D. Thesis, Universitá degli Studi di Napoli, Napoli, Italy, March 2000.

[30] Kosiwczuk, W., Cessou, A., Trinité, M., and Lecordier, B., "Simultaneous Velocity Field Measurements in Two-Phase Flows for Turbulent Mixing of Sprays by Means of Two-Phase PIV," *Experiments in Fluids*, Vol. 39, No. 5, 2005, pp. 895–908. doi:10.1007/s00348-005-0027-3

[31] Kosiwczuk, W., Cessou, A., Lecordier, B., and Trinité, M., "Simultaneous Velocity Field Measurements in Two-Phase Flows for Turbulent Mixing of Sprays by Means of Two-Phase PIV," Korea Maritime Univ. Paper 3229, Sept. 2003.

[32] Tóth, B., and Anthoine, J., "Two-Phase Flow PIV Experiments in a Solid Rocket Motor Model," The Calouste Gulbenkian Foundation, Paper 1320, July 2008.

K. Frendi
Associate Editor